This is a preprint, the final version is subject to change, of the American Mineralogist (MSA)
Cite as Authors (Year) Title. American Mineralogist, in press.
(DOI will not work until issue is live.) DOI: http://dx.doi.org/10.2138/am-2017-5871

Revision 1

Phase relations of $MgFe_2O_4$ at conditions of the deep upper mantle and transition zone

LAURA UENVER-THIELE[1], ALAN B. WOODLAND[1], TIZIANA BOFFA BALLARAN[2], NOBUYOSHI MIYAJIMA[2] AND DAN J. FROST[2]

[1] Institut für Geowissenschaften, Goethe-Universität Frankfurt, Altenhöferallee 1, D - 60438 Frankfurt am Main, Germany

[2] Bayerisches Geoinstitut, Universität Bayreuth, D - 95440 Bayreuth, Germany

Keywords: magnesioferrite, $MgFe_2O_4$, $Mg_2Fe_2O_5$, deep upper mantle, transition zone, high pressure

ABSTRACT

Phase relations of magnesioferrite ($MgFe_2O_4$) have been studied between 8 and 18 GPa and 1000-1600 °C using multi-anvil experiments. At 8-10 GPa and 900-1200 °C, $MgFe_2O_4$ breaks down to Fe_2O_3 + MgO. At higher temperatures, a new phase appears along with Fe_2O_3. Although this new phase is unquenchable, EPMA and TEM data point to a composition with

This is a preprint, the final version is subject to change, of the American Mineralogist (MSA)
Cite as Authors (Year) Title. American Mineralogist, in press.
(DOI will not work until issue is live.) DOI: http://dx.doi.org/10.2138/am-2017-5871

$Mg_5Fe_2O_8$ or $Mg_4Fe_2O_7$ stoichiometry. Depending on pressure and temperature, other stoichiometries also appear to be stable together with Fe_2O_3. In terms of pressure, the stability field of the unquenchable phases + hematite widens with increasing temperature to 3 ± 1 GPa at ~1400 °C, and then narrows to ~1 GPa at 1600 °C. The recoverable assemblage of $Mg_2Fe_2O_5$ + Fe_2O_3 becomes stable between 11-13 GPa. The $Mg_2Fe_2O_5$ + Fe_2O_3 assemblage is stable up to at least 18 GPa at 1300°C without any evidence of a hP-$MgFe_2O_4$ phase. In addition, hematite plays an important role in the phase relations of $MgFe_2O_4$ by being present over a wide range in pressure and temperature together with a Mg-rich Fe-oxide. Interestingly, hematite incorporates variable amounts of Mg whereby its concentration appears to be a function of temperature. This experimental study has implications for interpreting inclusions in natural diamonds where magnesioferrite occurs by placing a maximum pressure stability on the formation of this phase. Through these inclusions, it also provides constraints on diamond formation and their subsequent evolution prior to eruption. For example, the occasional observation of nano-sized magnesioferrite within (Mg,Fe)O inclusions must have either formed from a high-pressure precursor phase with a different stoichiometry at transition zone or upper lower mantle conditions, or it exsolved directly from the host (Mg,Fe)O under upper mantle conditions (i.e. < 9-10 GPa). Since a number of studies report a variety of non-silicate inclusions with simple oxide compositions, including magnesioferrite, magnetite or ferropericlase, such inclusions provide evidence for variable redox conditions at the time of entrapment.

INTRODUCTION

This is a preprint, the final version is subject to change, of the American Mineralogist (MSA)
Cite as Authors (Year) Title. American Mineralogist, in press.
(DOI will not work until issue is live.) DOI: http://dx.doi.org/10.2138/am-2017-5871

Spinel structured minerals with the chemical formula AB_2O_4 are of particular interest in having the ability to incorporate ferric (Fe^{3+}) and ferrous (Fe^{2+}) cations into their structure, which makes their stability sensitive to redox conditions. Such phases commonly occur in the peridotitic upper mantle and transition zone. Magnesioferrite ($MgFe^{3+}{}_2O_4$) is an example of such Fe^{3+}-bearing end member components that may be stable at such high pressure and temperature conditions. $MgFe_2O_4$ exhibits a cubic crystal structure (space group *Fd*-3*m*) with one tetrahedral and two octahedral sites per AB_2O_4 formula unit.

The high-pressure behavior of a number of spinel group minerals has been experimentally investigated over the last few decades, with a main interest being the nature of the "post-spinel" phase at conditions of the deep upper mantle and transition zone (e.g. Huang and Bassett 1986; Akaogi et al. 1999; Wang et al. 2003; Levy et al. 2004; Schollenbruch et al. 2010; Woodland et al. 2012; Ono et al. 2006; Kyono et al. 2012; Enomoto et al. 2009; Ishii et al. 2014, 2015). Apart from experimental studies, mineral inclusions in diamonds brought up to the surface provide a direct window into the Earth's interior. Thus, minerals entrapped by diamond represent a local part of the Earth's mantle. But interpreting the chemical signatures of these minerals can be hampered by fractures in diamond, which allows metasomatic interactions and/or changes in redox state. Additionally, high pressure-temperature phases can also decompose during upwelling.

With regard to spinel group minerals, it has been reported that they transform into denser orthorhombic structures of $CaFe_2O_4$ (*Pnma*), $CaTi_2O_4$ (*Cmcm*) or $CaMn_2O_4$ (*Pbcm*) type at high pressures (e.g. Andrault and Bolfan-Casanova, 2001; Yamanaka et al. 2008) or disproportionate. For example, at ~10 GPa and 700-1400 °C magnetite ($FeFe_2O_4$) breaks down to Fe_4O_5 + Fe_2O_3 (Woodland et al. 2012), while hercynite ($FeAl_2O_4$) and spinel ($MgAl_2O_4$) decompose into their constituent oxides (Schollenbruch et al. 2009; Akaogi et al. 1999). Andrault and Bolfan-

Casanova (2001) studied magnesioferrite by in situ X-ray diffraction at high pressures (> 20 GPa) using YAG laser annealing in a diamond anvil cell and reported a phase transformation at ~25 GPa, apparently to a $CaMn_2O_4$-type polymorph. Combining their P-V-T data on magnesioferrite with available thermodynamic data, Levy et al. (2004) proposed a phase diagram for $MgFe_2O_4$ that included a large stability field of $MgO + Fe_2O_3$ at intermediate pressure and temperature conditions, together with an assumed field of a hP-$MgFe_2O_4$ phase at P > 17 GPa. However, Levy et al. (2004) never produced the hP-$MgFe_2O_4$ phase and they had no direct experimental evidence for the existence of a $MgO + Fe_2O_3$ stability field at room temperature even up to 35 GPa.

In natural samples, magnesioferrite has been identified in ferropericlase inclusions occurring in diamond (Harte et al. 1999; Wirth et al., 2014). From their TEM observations, Wirth et al. (2014) suggested that the magnesioferrite might have previously been a hP-$MgFe_2O_4$ phase, formed by exsolution from an Fe^{3+}-bearing (Mg,Fe)O host during decompression enroute from the lower mantle. However, such an interpretation is dependent on the high-pressure phase relations of $MgFe_2O_4$, which are currently only poorly constrained as just described.

The discovery of new oxides with M_4O_5 stoichiometry (Enomoto et al. 2009, Lavina et al. 2011, Woodland et al. 2012, Ishii et al. 2014, 2015; Myhill et al. 2016) opens the possibility that analogous behavior may occur in the Mg-Fe^{3+}-system. In fact, complete substitution of Mg into Fe_4O_5, producing the new oxide phase $Mg_2Fe_2O_5$ has been recently reported (Boffa Ballaran et al., 2015). This phase exhibits the $CaFe_3O_5$-type structure (Boffa Ballaran et al., 2015). Considering the phase relations of other simple oxides, the stability of $Mg_2Fe_2O_5$ may also have implications for the $MgFe_2O_4$ system. Thus, our experimental study aims to investigate the phase relations of magnesioferrite at high pressures and temperatures to (1) identify the conditions for the breakdown of magnesioferrite, (2) verify the stability of a possible hP-$MgFe_2O_4$ phase and (3)

This is a preprint, the final version is subject to change, of the American Mineralogist (MSA)
Cite as Authors (Year) Title. American Mineralogist, in press.
(DOI will not work until issue is live.) DOI: http://dx.doi.org/10.2138/am-2017-5871

to assess whether $Mg_2Fe_2O_5$ is relevant to the $MgFe_2O_4$ bulk composition. Considering the occurrence of magnesioferrite in diamonds (e.g. Harte et al. 1999; Wirth et al. 2014), we then go on to briefly discuss the implications of our results for the Earth's upper mantle and transition zone.

EXPERIMENTAL METHODS

Starting materials

Stoichiometric mixtures of Fe_2O_3 and MgO or pre-synthesized magnesioferrite were used for high-pressure experiments (Table 1). Fe_2O_3 and MgO were pre-sintered in air at 1000 °C. For synthesizing $MgFe_2O_4$ a stoichiometric mixture of Fe_2O_3 and MgO was ground together and pressed into pellets and sintered in air in a muffle furnace (at 1atm) at 1000 °C for 40 hrs. After regrinding and repressing into pellets, the sample was sintered again at 1000 °C for 24 hrs, then at 950 °C (24 hrs), followed by a final cycle at 900 °C (24 hrs). The sample was then removed from the furnace and allowed to cool to room temperature. The resulting product was fine grained and had a light reddish-brown color. Several fragments were analyzed by electron microprobe (EPMA) to verify homogeneity and composition. X-ray powder diffraction revealed virtually pure magnesioferrite with a unit-cell parameter of a_o = 8.3875(1) Å with only a minor trace of Fe_2O_3. Comparing with the results of O'Neill et al. (1992), this unit-cell parameter indicates a stoichiometric composition with a degree of inversion of x = 0.84.

Experimental procedure

High pressure-temperature experiments were performed at the University of Frankfurt and the Bayerisches Geoinstitut, Bayreuth over a P-T range of 8-18 GPa and 900-1600 °C (see Table 1). Individual run conditions are presented in Table 1. The experiments performed at the University of Frankfurt were conducted in an 800t Walker-type multi-anvil apparatus (Walker et al. 1990) giving maximum load pressure of 14 GPa. Pressure calibration as well as the cell assembly design are described in detail by Brey et al. (2008). Experiments carried out at the Bayerisches Geoinstitut Bayreuth were performed using 500t, 1000t and 5000t multi-anvil presses. The pressure calibration and setup of those multi-anvil presses are reported in Keppler and Frost (2005). The assembly at the University of Frankfurt uses Re-foil as a heater, whilst $LaCrO_3$ is employed as heater at the Bayerisches Geoinstitut. The temperature was monitored by W_3/Re_{97}–W_{25}/Re_{75} thermocouples with the electromotive force uncorrected for pressure. Uncertainties in pressure and temperature are ±0.5 GPa and ±30-50 °C, respectively (Keppler and Frost 2005).

Sample powders were packed into capsules made from Pt foil, along with a small amount of PtO_2 placed at the bottom and/or the top of the capsule in order to keep the oxygen fugacity (fO_2) high during the experiment. At such a high fO_2, Fe-loss to Pt metal is negligible. Pieces of Pt-foil were placed between the starting material and the PtO_2 to minimize direct contact. In earlier experiments, we found that Pt can be locally incorporated in our oxide phases, when PtO_2 was in direct contact with our starting materials. In some experiments two capsules could be employed, allowing the simultaneous use of two different starting materials to directly monitor reaction direction (see Table 1).

Experiments followed the standard procedure of cold pressurizing, with subsequent heating to the desired temperature at a rate of ~50 °C/min. Isobaric quenching of the experiments

This is a preprint, the final version is subject to change, of the American Mineralogist (MSA)
Cite as Authors (Year) Title. American Mineralogist, in press.
(DOI will not work until issue is live.) DOI: http://dx.doi.org/10.2138/am-2017-5871

was achieved by turning off the power to the furnace, after which the sample was decompressed. The cooling rate was ~200-250 °C s^{-1}.

ANALYTICAL METHODS

Run products were analyzed by EPMA, powder X-ray diffraction and/or transmission electron microscopy (TEM). A few fragments of each sample were mounted in epoxy, polished and carbon coated for microprobe analysis. Measurements were carried out with a five-spectrometer JEOL JXA-8900 superprobe at the University of Frankfurt. Pure MgO, Fe_2O_3 and Pt metal were employed as primary standards. A CITZAF algorithm was used for matrix correction (Armstrong 1993). Measurements were performed in wavelength-dispersive mode using 15 kV accelerating voltage, a beam current of 20 nA and a beam spot size of 1μm. Integration times for Fe and Pt were 40 s on the peak and 20 s on background. An integration time of 40 s on the peak and background was adjusted for Mg. Backscattered electron images were taken to investigate microtextures and to verify homogeneity of the mineral grains. If the grains were large enough (>20 μm), 3-5 points were measured on a single grain.

Further phase identification was performed with X-ray powder diffraction patterns that were collected on two diffractometers. One was a Philips X´Pert PRO diffractometer at the Bayerisches Geoinstitut, Bayreuth using monochromatic Co Kα (λ = 1.78897 Å) radiation selected with a focusing monochromator, a symmetrically cut curved Johansson Ge (111) crystal and equipped with a Philips X'celerator detector. Silicon (NIST SRM 640c) was added as an internal standard. Data were collected between 10° and 120° 2 θ at 40 kV and 40 mA. Other patterns were collected with a STOE Stadi P diffractometer at the University of Frankfurt operating at 45 kV and 35 mA and using monochromatic Mo Kα (λ = 0.70926 Å) radiation,

along with a linear PSD or a Mythen detector. In this later case, the sample material containing a Si internal standard (cross-calibrated with the standard in Bayreuth) was mounted in a 0.5 mm diameter capillary and measured in transmission mode between 1°-100° 2 θ. Unit-cell parameters were determined from full-pattern Rietveld refinements using the General Structure Analysis System (GSAS, Larson and van Dreele 1994) software package and the EXPGUI interface of Toby (2001).

TEM analysis was carried out using FEI Titan G2 80-200 S/TEM equipped with 4 SDD energy-dispersive X-ray spectrometers, operated at 200 kV. One of the recovered samples (M568) was cut and polished to make a thin section. The thin section was mounted on a Mo grid and Ar-ion milled to electron transparency at accelerating voltages of 4.0 kV with an incident angle of 8° using a precision ion polishing system (Gatan, model 691). The sample foil was coated with amorphous carbon in order to reduce charging.

RESULTS AND DISCUSSION

The use of different starting mixtures permitted us to demonstrate the direction of reaction and, thus to determine the stable phase assemblage at the conditions of a given experiment (Table 1). Broadly using the proposed phase diagram of Levy et al. (2004), we employed either $MgFe_2O_4$ or stoichiometric mixtures of $MgO + Fe_2O_3$ to unequivocally demonstrate which assemblage was stable at a given pressure and temperature. In a number of cases, two separate capsules with different starting materials were included in a single experiment. In other cases, 10% $MgFe_2O_4$ was mixed together with $MgO + Fe_2O_3$ to minimize potential kinetic problems related to nucleation of magnesioferrite from an oxide mixture. The direction of reaction could

185 then be monitored from the relative phase proportions determined from refinement of the X-ray
186 diffraction pattern.

187 Depending on the pressure and temperature of the experiment, the duration varied from
188 1.5-24 hrs (see Table 1). Backscattered electron imaging of the run products confirms significant
189 grain growth and essentially complete recrystallization. Most samples revealed homogenous and
190 well-crystalized grains, whereas a number of experiments (e.g. M553, M568, V841o; Table 1)
191 contained grains that exhibited extremely fine-grained internal textures, suggesting reaction had
192 occurred during quenching (see below). Stoichiometric calculations based upon microprobe
193 analyses indicate that, with the help of a little PtO_2, the oxygen fugacity had been kept high
194 enough so that the iron remained in the ferric state for the duration of the experiments. At such
195 oxidizing conditions, incorporation of Pt into the oxide phases needed to be monitored, as
196 hematite with up to ~7 wt% PtO_2 or $MgFe_2O_4$ with up to 1 wt% were observed in a few samples,
197 for crystals in direct contact with PtO_2. Such samples were not considered when assessing the
198 phase relations of $MgFe_2O_4$. No measureable or only traces of Pt were observed in either
199 ferropericlase or the new $Mg_2Fe_2O_5$ phase (Table 2). Magnesite appeared in trace quantities in a
200 number of samples (see Table 1, 2). This was possibly introduced into the experiments as
201 adsorbed CO_2 on the PtO_2 powder, which has a very fine grain size. Although the presence of
202 magnesite alters the bulk composition, the small amounts should have negligible effect on the
203 stability of the coexisting oxide phases.
204
205 **The breakdown of $MgFe_2O_4$ at low temperatures**
206
207 At 8-10 GPa and temperatures of 900-1200 °C $MgFe_2O_4$ was observed to breakdown to
208 its constituent oxide phases according to the reaction:

209 $$MgFe_2O_4 = MgO + Fe_2O_3 \quad (1)$$

210 mf per hem

211 Backscatter electron images reveal that where magnesioferrite was stable, it produced
212 grains up to 150 μm in size, whereas mixtures of MgO and Fe_2O_3 were much finer grained (~10
213 μm, compare Fig. 1a and 1b). The measured cell parameter for periclase in our experiments
214 agrees with the value of a_o = 4.2110 Å reported for MgO by Hazen (1976) (Table 3). The
215 position of the phase boundary can be described by the following equation (see Fig. 2):

216

217 $$P\ [\text{GPa}] = 6.7\text{x}10^{-3} \text{ x } T\ [^\circ\text{C}] + 1.8$$

218

219 The boundary computed by Levy et al. (2004) lies at significantly higher pressures. On
220 the other hand, the database of Holland and Powell (2011) seems to reproduce our results
221 reasonably well, even if their slope is much steeper than that implied from our data.

222

223 **$MgFe_2O_4$ breakdown at higher temperature**

224

225 At temperatures > 1200 °C and 9-10 GPa, $MgFe_2O_4$ no longer breaks down directly to
226 MgO + Fe_2O_3. Although the powder diffraction patterns often contain peaks consistent with
227 hematite, MgO and $MgFe_2O_4$, the peaks are broad and difficult to refine, suggesting that these
228 phases are poorly crystalline or of extremely fine grain size. Furthermore, there are additional
229 diffraction peaks that do not belong to any of these phases. In these cases, estimated phase
230 proportions of MgO and Fe_2O_3 are significantly different from those observed in the lower
231 temperature experiments. Following the phase diagram of Levy et al. (2004), a transformation to
232 hp-$MgFe_2O_4$ would be expected. However, neither our microprobe analyses nor our powder

diffraction patterns are consistent with a high-pressure polymorph being present. The orthorhombic structures frequently encountered in post-spinel transitions (i.e. the $CaFe_2O_4$, $CaTi_2O_4$ and $CaMn_2O_4$-type structures), tetragonally distorted structures (e.g. Yong et al. 2012; Kyono et al. 2012) proved to be inconsistent with our data. The diffraction peaks also cannot be fitted with the $Mg_2Fe_2O_5$ structure (Boffa Ballaran et al. 2015). Nevertheless, XRD patterns and microprobe analyses of the run products confirm the breakdown of $MgFe_2O_4$ at pressures of ~9-10 GPa ± 0.5 GPa and temperatures > 1200 °C (Table 1, 2, Fig. 3).

An important characteristic of the run products in this pressure-temperature range is their texture, as revealed by BSE-imaging. They are marked by the presence of coarse-grained hematite coexisting with another phase that clearly has a much lower mean atomic number (Fig. 4a). The presence of well-developed triple junctions provides textural evidence for equilibrium conditions in these experiments (Fig. 4a, 4b). In many cases, the additional phase can also be quite coarse-grained (> 100 μm, Fig. 4b), even though the grains themselves have a very fine internal structure (Fig. 4b, 4c). Thus, it appears that this phase has decomposed or at least partially decomposed either during temperature quenching or decompression. The coexistence of hematite in the experiments indicates that this phase must have been substantially richer in Mg than the $MgFe_2O_4$ starting composition. We can rule out $Mg_2Fe_2O_5$ since it is known to be recoverable from 15 GPa and ~1550 °C and there is no reason to suspect that its behavior should be different at somewhat lower pressures (Boffa-Ballaran et al. 2015). In spite of its unquenchable nature, the resultant very fine grain size of the mixture (<< 1 μm and see below) means that microprobe analyses average over a significant volume and can give an indication of the composition of the original phase. In fact, for a given sample multiple microprobe analyses yield consistent compositions, reproducible within ± 1-2 wt%. For example, compositions of 50.5

wt% MgO and 44.6 wt% FeO (sample M551) and 55.9 wt% MgO and 41.6 wt% FeO (sample M568) suggest stoichiometries for the unquenchable phase of $Mg_4Fe_2O_7$ and $Mg_5Fe_2O_8$, respectively, when charge balance is assumed (Table 4). This assessment also indicates that Fe was maintained in the ferric state during the experiments through the presence of the PtO_2. These derived compositions are also inconsistent with the $Mg_2Fe_2O_5$ stoichiometry (Table 4).

Sample M568 was investigated by TEM in order to obtain additional compositional and textural information about the unquenchable phase. Dark field images reveal a vermicular intergrowth of two phases at the scale of ~10 nm consistent with spinodal decomposition as suspected from the BSE images (Fig. 5a). STEM-EDX chemical mapping yields two distinct chemical domains: a Fe-rich domain with a composition corresponding to $MgFe_2O_4$ and a Fe-poor domain, much richer in Mg (Fig. 5b). Electron diffraction patterns made by Fast Fourier Transforms (FFT) in the HRTEM of the Fe-rich domains confirm a cubic spinel structure (Fig. 5c) consistent with the measured $MgFe_2O_4$ composition, while the Mg-rich domains exhibit a rock salt structure, as expected for MgO (Fig. 5d). Results of chemical mapping over the large area yield a bulk composition of $Mg_5Fe_2O_8$, which agrees with the microprobe measurement for this sample (Table 2 and 4).

Since we cannot definitively identify the structure and composition of this Mg-rich phase or phases stable at high temperatures and pressures, we informally refer to it as an "unquenchable" phase (UQ). Thus, we propose that $MgFe_2O_4$ breaks down to an assemblage of hematite and an unquenchable Mg-Fe oxide with an original stoichiometry of e.g. $Mg_4Fe_2O_7$ or $Mg_5Fe_2O_8$ depending on the exact pressure and temperature of the experiment. In our phase diagram, we have chosen to lump this region together into a single field, even though in detail more than one Mg-rich phase may be stable in this region (Fig. 3). In fact, a variety of hypothetical compositions can be considered that can be matched up with observed bulk

280 microprobe analyses (Table 4, Fig. 6, 7). The coexistence of a particular phase stoichiometry with
281 hematite requires that all other phases lying in between are unstable at the given pressure and
282 temperature. Two experiments (M630, M632; Table 1) also exhibit an unquenchable phase
283 coexisting with hematite, but yield a composition anomalously high in Mg (i.e. ~76 wt % MgO
284 and ~24 wt % FeO; Table 2). This composition would imply a $Mg_{11}Fe_2O_{14}$ stoichiometry and is
285 consistent with the qualitatively higher proportion of coexisting hematite in these samples
286 compared with those containing other unquenchable phases. Considering the distribution of the
287 different stoichiometries as a function of pressure and temperature (Table 1), the unquenchable
288 phase appears to exhibit a general decrease in Mg content with increasing temperature, away
289 from the MgO + Fe_2O_3 stability field. However a more precise analysis is precluded by the
290 inherent uncertainties in the pressure and temperature of the individual experiments (see above).
291 Although the exact nature of the unquenchable phases remains unknown, our experiments at ~ 10
292 GPa and above 1200 °C demonstrate that the boundary delineating the $MgFe_2O_4$ breakdown
293 reaction is virtually isobaric (Fig. 3). In situ measurements will be necessary to provide more
294 precise information about the true nature of the Mg-Fe oxides stable above ~10 GPa.

295

296 **Stability of $Mg_2Fe_2O_5$ + Fe_2O_3**

297

298 The stability field for the unquenchable phases and hematite is rather narrow in terms of
299 pressure, giving way to the recoverable assemblage of $Mg_2Fe_2O_5$ + Fe_2O_3 (Fig. 3, Table 1). This
300 field was not foreseen by Levy et al. (2004). $Mg_2Fe_2O_5$ is isostructural with Fe_4O_5 (Boffa
301 Ballaran et al. 2015) and is easily distinguishable from other phases in X-ray powder diffraction
302 patterns (Fig. 8). The unit-cell parameters are given in Table 5 and are very similar to those

303 published for the Mg-endmember $Mg_2Fe_2O_5$ in Boffa-Ballaran et al. (2015). This implies little or
304 only minor reduction of ferric to ferrous iron. The occurrence of large crystals in some samples
305 compared to other assemblages (Fig. 1a, 1b) demonstrates its quenchable nature without any
306 apparent spinodal-like texture. With increasing pressure, $Mg_2Fe_2O_5 + Fe_2O_3$ becomes stable to
307 lower temperatures at the expense of $MgO + Fe_2O_3$ indicating this boundary has a negative slope
308 (Fig. 3). The $Mg_2Fe_2O_5 + Fe_2O_3$ assemblage is stable up to at least 18 GPa, with additional
309 experiments underway to investigate the full breadth of its stability field.

310

311 **High-pressure behavior of hematite**

312

313 The phase relations of magnesioferrite as depicted in Figure 3 demonstrate that hematite
314 plays an important role in post-spinel assemblages. It occurs with a variety of phases that always
315 have a higher Mg/Fe^{3+} than that present in $MgFe_2O_4$. The coexistence of hematite also implies
316 that no other phases with lower Mg/Fe^{3+} (i.e. a Mg-bearing solid solution of $Fe_{13}O_{19}$; Merlini et
317 al. 2015) are stable within the pressure and temperature range of our experiments. However, at
318 such high pressures the hematite is not pure Fe_2O_3, but was found to incorporate up to ~3.5 wt%
319 MgO (≙0.135 c.p.f.u.). This is not an analytical artifact since we observe Mg contents to increase
320 with increasing temperature of the experiment (Fig. 9a). In addition, the lattice parameters and
321 molar volume systematically change with measured Mg concentration (Table 6, Figs. 9b, 9c, 9d).
322 The substitution of divalent Mg for Fe^{3+} can be understood in terms of a Mg_3O_3 component,
323 where two Fe^{3+} cations are replaced by Mg and an additional Mg cation occupies a normally
324 adjacent vacant site in the crystal structure (Berry et al. 1998, 2000). Whilst α- Fe_2O_3 has pairs of
325 face-sharing FeO_6 octahedra along [001], the incorporation of Mg leads to the formation of

326 triplets along the same crystallographic direction. In this way charge balance is maintained, but
327 stoichiometry deviates from the ideal two cations per three oxygens through the presence of
328 interstitial Mg (Table 6). Our data set is in good agreement with this structural model in so far as
329 the observed expansion along the *c*-axis is about twice that along the *a*-axis (see Figs. 9c and 8d).
330 The maximum extent of non-stoichiometry reaches 2.045 cations on a three-oxygen basis (Table
331 6), which should act to stabilize the assemblage hematite + MgO. As a result, we would expect
332 the phase boundary between $MgFe_2O_4$ and this assemblage to shift to lower pressures. However,
333 hematite in this range of pressure and temperature contains less Mg, reaching a maximum non-
334 stoichiometry of 2.019 cations on a three-oxygen basis in sample M588 (Table 6). Assuming that
335 Raoult's law is valid over this small compositional range (mole fraction of hematite = 0.981), we
336 can estimate the effect of solid solution on the position of the phase boundary. In this case, the
337 free energy difference amounts to only several hundred joules, which implies a shift of < 0.1
338 GPa. Thus, this effect cannot account for the observed discrepancy between our results for
339 equilibrium (1) and the calculations of Levy et al. (2004).

340

341 **Comparison with other Mg and Fe-bearing oxide systems**

342

343 Aside from ringwoodite, mantle-derived spinels have major element compositions
344 dominated by Mg and Fe^{2+}, along with Fe^{3+}, Cr and/or Al as trivalent cations. Therefore, it is of
345 interest to compare the phase relations in different endmember systems in order to predict the
346 behavior of more complex solid solutions and to understand how the incorporation of certain
347 cations may affect phase stabilities. We have demonstrated that the phase relations for $MgFe_2O_4$
348 are rather more complicated than proposed by Levy et al. (2004). At about 9 GPa and

349 temperatures up to 1200 °C, $MgFe_2O_4$ breaks down to its constituent oxides: MgO + Fe_2O_3. This
350 contrasts with the Mg-free analog $FeFe_2O_4$, where no such field has been observed
351 (Schollenbruch et al. 2011; Huang and Bassett 1986). Instead, magnetite breaks down at 9.5-11
352 GPa and 700-1400 °C by undergoing a disproportionation reaction to Fe_4O_5 + Fe_2O_3 (Woodland
353 et al. 2012). In the $MgFe_2O_4$ system, $Mg_2Fe_2O_5$ + Fe_2O_3 does become stable at somewhat higher
354 pressures (Fig. 3, 10), but magnesioferrite does not directly break down to this assemblage. In
355 this case, there is an intervening field involving one or more unquenchable Mg-Fe oxides that
356 appear to have more complex stoichiometries (see above). Thus, substitution of Mg for Fe^{2+} in
357 the presence of Fe^{3+} does not just lead to a shift in phase boundaries to different pressures and
358 temperatures, but it alters the phase relations by stabilizing additional phase fields. On the other
359 hand, it is notable that the high-pressure stabilities of magnesioferrite and magnetite are similar
360 (they lie within a couple of GPa at a given temperature, see Fig. 10).

361 In Cr-bearing compositions, phase relations exhibit similarities and differences compared
362 to the Fe^{3+}-bearing endmembers (Fig. 10). Recent studies on chromite ($FeCr_2O_4$) and
363 magnesiochromite ($MgCr_2O_4$) by Ishii et al. (2014, 2015) also highlight the influence of Mg^{2+} on
364 the phase relations of Cr-spinels. In a fashion analogous to magnetite, chromite breaks down to
365 $Fe_2Cr_2O_5$ + Cr_2O_3, although $Fe_2Cr_2O_5$ has apparently a slightly different crystal structure than
366 that observed for Fe_4O_5. Magnesiochromite reacts directly to $Mg_2Cr_2O_5$ + Cr_2O_3 (Ishii et al.
367 2015), without any intermediate phase field, which contrasts with that observed for $MgFe_2O_4$. On
368 the other hand, $MgCr_2O_4$ also breaks down to its constituent oxides at low temperatures, like
369 $MgFe_2O_4$ does. Such a phase field is clearly not favored in Fe^{2+}-bearing endmembers regardless
370 of whether Fe^{3+} or Cr is the trivalent cation. The high-pressure stability limits of chromite and
371 magnesiochromite are nearly identical (Fig. 10, Ishii et al. 2014, 2015) and lie 2-5 GPa higher
372 than those for the Fe^{3+}-bearing spinel phases.

The Mg-bearing spinel, $MgAl_2O_4$, exhibits different phase relations in that it breaks down to its constituent oxides ($MgO + Al_2O_3$) at 15-16 GPa and over a wide range of temperatures (1000-1600°C, Liu 1975; Akaogi et al. 1999). At temperatures > 1900°C, Enomoto et al. (2009) reported that $MgO + Al_2O_3$ reacts to form the assemblage $Mg_2Al_2O_5 + Al_2O_3$ at 20-26 GPa. These relations are not unlike those observed for $MgFe_2O_4$ (Fig. 3, 10) and $MgCr_2O_4$ (Ishii et al. 2015), albeit with the different phase fields occurring at much higher temperatures. As illustrated in Figure 10, the maximum pressure stabilities of the Mg-bearing spinel-structured phases in their respective systems have the following sequence: $MgAl_2O_4 > MgCr_2O_4 > MgFe_2O_4$.

The Fe^{2+} bearing analog to spinel, hercynite ($FeAl_2O_4$), disproportionates into a mixture of corundum and wüstite at 7–8.5 GPa and temperatures of 900-1700 °C (Schollenbruch et al. 2009). The constituent oxides remain stable up to at least 24 GPa and 1700 °C, with no evidence for a $Fe_2Al_2O_5$ phase becoming stable. However, considering the results of Enomoto et al. (2009), it is still possible that an assemblage of $Fe_2Al_2O_5 + Al_2O_3$ might be stable above 1700 °C. Comparison of the Fe^{2+}-bearing systems reveals that the sequence of maximum pressure stability for the spinel-structured phases is $FeCr_2O_4 > FeFe_2O_4 > FeAl_2O_4$, which is quite different from that of the Mg-bearing analogs (Fig. 10).

IMPLICATIONS FOR THE MANTLE

Studies of inclusions in diamonds provide direct information about the conditions and composition of the Earth's deep interior, at least of the local domain in which a diamond crystallized. For example, inclusions can potentially give evidence for the prevailing pressure-temperature, and possibly oxygen fugacity conditions during entrapment. A number of studies

report a variety of non-silicate inclusions with simple oxide compositions, including magnetite, wüstite and metallic Fe (e.g. Meyer 1987; Stachel et al. 1998). Their occurrence together in a single diamond emphasizes the fact that diamond formation may take place in a significant redox gradient (Stachel et al. 1998).

Inclusions of (Mg,Fe)O in diamond are often considered to indicate a deep origin in the lower mantle (e.g. Harte et al. 1999). Samples from Juina Province, Brazil are particularly noteworthy in that the inclusions also contain nm-sized magnesioferrite (Harte et al. 1999; Wirth et al. 2014; Kaminsky et al. 2015; Palot et al. 2016). In their TEM study, Wirth et al. (2014) identified platelets of $(Mg_{0.5}Fe_{0.5})Fe_2O_4$ occurring along dislocations or at the diamond-inclusion interface. In addition, magnetite, Al-bearing spinel and a Fe-Ni alloy were also found to occur within the host inclusion. The observed microtextures were interpreted by Wirth et al. (2014) as indicating that $(Mg_{0.5}Fe_{0.5})Fe_2O_4$ originally formed as a high-pressure polymorph that reverted to magnesioferrite during decompression. Palot et al. (2016) also reported magnesioferrite with an approximate composition of $Mg(Fe_{0.75},Cr_{0.17},Al_{0.08})_2O_4$ decorating dislocations and occurring as 10-20 nm euhedral crystals within another (Mg,Fe)O included in diamond from the same location. Based upon a phase diagram valid for 1 atm, they considered this phase to have formed during uplift, but still within the lower mantle at pressures > 25 GPa. Furthermore, the occurrence of euhedral precipitates was interpreted as indicating that the magnesioferrite formed directly from the ferropericlase host. However, our phase relations presented in Figure 3 and Figure 10 demonstrate that 1) magnesioferrite is not stable at such pressures and 2) magnesioferrite does not directly transform into a high-pressure polymorph, hp-$MgFe_2O_4$ not being stable up to 18 GPa, at least at 1300 °C. Such a hp-$MgFe_2O_4$ phase may be stable at still higher pressures, as reported by Andrault and Bolfan-Casanova (2001). However, there must be an intervening stability field with the assemblage "O_5" phase + sesquioxide solid solution (i.e. a Fe_2O_3-rich

phase) between the fields of magnesioferrite and the high-pressure polymorph. This is also the case for Cr-bearing compositions (Fig. 10, Ishii et al. 2014, 2015). It is important to note that Wirth et al. (2014) reported the presence of an additional, unidentifiable phase located between the magnesioferrite platelets, implying that the precursor had a stoichiometry different from that of spinel. An alternative interpretation could be that at transition zone conditions, $Mg_2Fe_2O_5$ initially exsolved from the host (Mg,Fe)O, and during upwelling subsequently reacted to one or other of our unquenchable Mg-Fe oxides (e.g. $Mg_4Fe_2O_7$ or $Mg_5Fe_2O_8$ etc.) before further reacting to magnesioferrite upon reaching its stability field in the upper mantle (i.e. 9-10 GPa).

The presence of magnesioferrite led both Wirth et al. (2014) and Palot et al. (2016) to propose that the original (Mg,Fe)O had a significant non-stoichiometry (i.e. Fe^{3+} content). However, such a degree of non-stoichiometry is inconsistent with experimental data (McCammon et al. 1998). Another possibility is in situ oxidation through reaction with a small amount of carbonate-bearing (fluid or a solid) that was trapped along with the (Mg,Fe)O inclusion. A coupled reaction of the form: 2 FeO (oxide) + CO_2 = C + Fe_2O_3 (oxide) would produce diamond together with ferric iron that would drive the formation of an additional phase such as $Mg_2Fe_2O_5$. In fact, Palot et al. (2016) report the coexistence of brucite in the host ferropericlase, providing direct evidence for the presence of a fluid. Carbonate inclusions have been reported in other diamonds from the same locality (Kaminsky et al. 2009, 2013), further supporting this possibility.

The mechanism of carbon-iron redox-coupling to produce diamond along with a coexisting Fe^{3+}-bearing phase does not have to be restricted to isolated inclusions, but can also have relevance for the diamond-formation process in general. Although they are not expected to be stable at the ambient oxidation state of the transition zone (i.e. near metal saturation, Frost and

McCammon, 2008), such Fe^{3+}-rich phases can develop locally where strong redox gradients attend diamond formation (Stachel et al. 1998). On the other hand, the many similarities between $MgFe_2O_4$ and other AB_2O_4 endmember systems (where A and B stand for divalent and trivalent cations, respectively) suggest phases like $A_2B_2O_5$ can form complex solid solutions involving trivalent cations other than Fe^{3+}. Such substitutions can act to expand the redox stability of these phases. So far unique to $MgFe_2O_4$ is the occurrence of Mg-Fe oxides with more complex stoichiometries like $Mg_4Fe_2O_7$ or $Mg_5Fe_2O_8$, or even $Mg_{11}Fe_2O_{14}$. Whether these phases can also form solid solutions awaits further study. Although Fe_5O_6 has been reported (Lavina & Meng 2015; Woodland et al. 2015), it is not a stable phase in a Fe_3O_4 bulk composition (Woodland et al. 2015). Interestingly, one of the unquenchable phases encountered at 10 GPa and 1500 °C had a $Mg_3Fe_2O_6$ stoichiometry, which would represent an analog to Fe_5O_6 (Table 1). Whether this Mg-endmember has a large stability field (or is quenchable) in more Mg-rich bulk compositions remains to be investigated.

Magnesioferrite and magnetite have very similar high-pressure stabilities, both breaking down at 9-10 GPa (Schollenbruch et al. 2011; Woodland et al. 2012). Although the phase relations of magnetite have received much attention over the years, no additional oxide phases with stoichiometries of e.g. $Mg_4Fe_2O_7$ or $Mg_5Fe_2O_8$ have been reported. The high pressure-temperature behavior of solid solutions along the $MgFe_2O_4$ – $FeFe_2O_4$ could be of further interest, in that their composition is more applicable for the Earth's mantle. Thus, an experimental study on the phase relations of $(Mg_{0.5}Fe_{0.5})Fe_2O_4$ similar to that identified by Wirth et al. (2014) in their ferropericlase inclusion is currently underway.

ACKNOWLEDGMENTS

This work was supported by the Deutsche Forschungsgemeinschaft through grants WO 652/20-1 and BO 2550/7-1 to ABW and TBB, respectively. E. Alig and H. Höfer are thanked for helping with the X-ray powder diffraction and microprobe measurements, respectively. The manuscript was improved through insightful comments from R. Myhill and an anonymous reviewer. Fruitful discussions with R. Angel and F. Brenker are gratefully acknowledged.

REFERENCES CITED

Akaogi, M., Hamada, Y., Suzuki, T., Kobayashi, M., and Okada, M. (1999) High pressure transitions in the system $MgAl_2O_4$–$CaAl_2O_4$: a new hexagonal aluminous phase with implication for the lower mantle. Physics of the Earth and Planetary Interiors, 115, 67–77.

Andrault, D., and Bolfan-Casanova, N. (2001) High-pressure phase transformations in the $MgFe_2O_4$ and Fe_2O_3-$MgSiO_3$ systems. Physics and Chemistry of Minerals. 28, 211-217.

Armstrong, J.T. (1993) Matrix correction program CITZAF, Version: 3.5, California Institute of Technology

Berry, F.J., Bohorquez, A., Greaves, C., McManus, J., Moore, E.A., and Mortimer, M. (1998) Structural characterization of divalent Magnesium-doped α-Fe_2O_3. Journal of Solid State Chemistry, 140, 428-430.

Berry, F.J., Greaves, C., Helgason, Ö., McManus, J., Palmer, H.M., and Williams, R.T. (2000) Structural and Magnetic Properties of Sn-, Ti-, and Mg-Substituted α-Fe_2O_3: A Study by Neutron Diffraction and Mössbauer Spectroscopy. Journal of Solid State Chemistry, 151, 157-162.

Boffa Ballaran, T., Uenver-Thiele, L., Woodland, A.B., and Frost, D.J. (2015) Complete substitution of Fe^{2+} by Mg in Fe_4O_5: The crystal structure of the $Mg_2Fe_2O_5$ end-member. American Mineralogist, 100, 628-632.

Enomoto, A., Kojitan,i H., Akaogi, M., Miura, H., and Yusa, H. (2009) High-pressure transitions in $MgAl_2O_4$ and a new high-pressure phase of $Mg_2Al_2O_5$. Journal of Solid State Chemistry, 182, 389–395.

Frost, D.J., and McCammon, C.A. (2008) The redox state of Earth's mantle. Annual Reviews of Earth and Planetary Sciences, 36, 389–420. doi:10.1146/Annurev.Earth.36.031207.124322

Hanrahan, M., Brey, G., Woodland, A., Altherr, R., and Seitz, H.-M. (2009) Towards a Li barometer for bimineralic eclogites: experiments in CMAS. Contributions to Mineralogy and Petrology, 158, 169–183.

Harte, B., Harris, J.W., Hutchison, M.T., Watt, G.R., and Wilding, M.C. (1999) Lower mantle mineral associations in diamonds from Sã̃o Luiz, Brazil. In: Mantle Petrology: Field Observations and High Pressure Experimentation. The Geochemical Society, Special Publication, 6, 125-153.

514 Hazen, R.M. (1976) Effects of temperature and pressure on the cell dimension and X-ray
515 temperature factors of periclase. American Mineralogist, 61, 266-271.
516
517 Holland, T.J.B., and Powell, R. (2011) An improved and extended internally consistent
518 thermodynamic dataset for phases of petrological interest, involving a new equation of state for
519 solids. Journal of Metamorphic Geology, 29, 333-383.
520
521 Huang, E., and Bassett, W.A. (1986) Rapid-determination of Fe_3O_4 phase-diagram by
522 synchrotron radiation. Journal of Geophysical Research, 91(B5), 4697–4703.
523
524 Ishii, T., Kojitani, H., Tsukamoto, S., Fujino, K., Mori, D., Inaguma, Y., Tsujino, N., Yoshino,
525 T., Yamazaki, D., Higo, Y., Funakoshi, K., and Akaogi, M. (2014) High-pressure phase
526 transitions in $FeCr_2O_4$ and structure analysis of new post-spinel $FeCr_2O_4$ and $Fe_2Cr_2O_5$ phases
527 with meteoritical and petrological implications. American Mineralogist, 99, 1788-1797.
528
529 Ishii, T., Kojitani, H., Fujino, K., Yusa, H., Mori, D., Inaguma, Y., Matsushita, Y., Yamaura, K.,
530 and Akaogi, M. (2015) High-pressure high-temperature transitions in $MgCr_2O_4$ and crystal
531 structures of new $Mg_2Cr_2O_5$ and post-spinel $MgCr_2O_4$ phases with implications for ultrahigh-
532 pressure chromitites in ophiolites. American Mineralogist, 100, 59-65.
533
534 Kaminsky, F., Wirth, R., Matsyuk, S., Schreiber, A., and Thomas, R. (2009) Nyerereite and
535 nahcolite inclusions in diamond: evidence for lower-mantle carbonatitic magmas. Mineralogical
536 Magazine, 73, 5, 797-816.
537

Kaminsky, F.V. (2013) Carbonatitic inclusions in deep mantle diamond from Juina, Brazil: New minerals in the carbonate-halide association. The Canadian Mineralogist, 51, 669-688.

Kaminsky, F.V., Ryabchikov, I.D., McCammon, C.A., Longo, M., Abakumov, A.M., Turnerd, S., and Heidari, H. (2015) Oxidation potential in the Earth's lower mantle as recorded by ferropericlase inclusions in diamond. Earth and Planetary Science Letters, 417, 49–56.

Keppler, H., and Frost, D.J. (2005) Introduction to minerals under extreme conditions. In: Miletich R. (Edt). Mineral Behaviour at Extreme Conditions. EMU Notes in Mineralogy. 7, 1-30.

Larson, A.C., and Von Dreele, R.B. (1994) GSAS General Structure Analysis System. Los Alamo National Laboratory, New Mexico, USA

Lavina, B., Dera, P., Kim, E., Meng, Y., Downs, R.T., Weck, P.F., Sutton, S.R, and Zhao, Y. (2011) Discovery of the recoverable high-pressure iron oxide Fe_4O_5. Proceedings of the National Academy of Sciences. 108, 17281-17285.

Lavina, B.,and Meng, Y. (2015) Unraveling the complexity of iron oxides at high pressure and temperature: Synthesis of Fe_5O_6. Science Advances 1:e1400260

Levy, D., Diella, V., Dapiaggi, M., Sani, A., Gemmi, M., and Pavese, A. (2004) Equation of state, structural behaviour and phase diagram of synthetic $MgFe_2O_4$, as a function of pressure and temperature. Physics and Chemistry of Minerals. 31, 122-129.

562 Liu, L.G. (1975) Disproportionation of $MgAl_2O_4$ spinel at high-pressure and temperature.
563 Geophysical Research Letters, 2, 9-11.
564
565 McCammon, C., Peyronneau, J., and Poirier, J.-P. (1998) Low ferric iron content of (Mg,Fe)O at
566 high pressures and temperatures. Geophysical Research Letters, 25, 1589-1592.
567
568 Merlini, M., Hanfland, M., Salamat, A., Petitgirard, S., Müller, H. (2015) The crystal structures
569 of $Mg_2Fe_2C_4O_{13}$, with tetrahedrally coordinated carbon, and Fe13O19, synthesized at deep
570 mantle conditions. American Mineralogist, 100, 2001-2004.
571
572 Meyer, H.O.A. (1987) Inclusions in diamond. In: Nixon P.H. ed., Mantle Xenoliths, John Wiley
573 and Sons, New York, 501-523.
574
575 Myhill, B., Ojwang, D.O., Ziberna, L., Frost, D., Boffa Ballaran, T., Miyamjima, N. (2016). On
576 the P-T-fO_2 stability of Fe4O5 and Fe5O6-rich phases: a thermodynamic and experimental study.
577 Contributions to Mineralogy and Petrology, 171, 5, 1-11.
578
579 Ono, S., Kikegawa, T., and Ohishi, Y. (2006) The stability and compressibility of $MgAl_2O_4$ high-
580 pressure polymorphs. Physics and Chemistry of Minerals, 33, 200-206.
581
582 O'Neill, H.St.C., Annersten, H., and Virgo, D. (1992) The temperature dependence of the cation
583 distribution of magnesioferrite ($MgFe_2O_4$) from powder XRD structural refinements and
584 Mössbauer spectroscopy. American Mineralogist, 77, 725-740.
585

Palot, M., Jacobsen, S.D., Townsend, J.P., Nestola, F., Marquardt, K., Miyajima, N., Harris, J.W., Stachel, T., McCammon, C.A., and Pearson, D.G. (2016) Evidence for H_2O-bearing fluids in the lower mantle from diamond inclusion. Lithos, in press.

Tobi, B.H. (2001) EXPGUI, a graphical user interface for GSAS. Journal of Applied Crystallography, 34, 210-213.

Schollenbruch, K., Woodland, A.B., and Frost, D.J. (2010) The stability of hercynite at high pressures and temperatures. Physics and Chemistry of Minerals, 37, 137-143.

Schollenbruch, K., Woodland, A.B., Frost, D.J., Wang, Y., Sanehira, T., and Langenhorst, F. (2011) In situ determination of the spinel–post-spinel transition in Fe_3O_4 at high pressure and temperature by synchrotron X-ray diffraction. American Mineralogist, 96, 820-827.

Wang, Z., Downs, R.T., Pischedda, V., Shetty, R., Saxena, S.K., Zha, C.S., Zhao, Y.S., Schiferl, D., and Waskowska, A. (2003) High-pressure x-ray diffraction and Raman spectroscopic studies of the tetragonal spinel $CoFe_2O_4$. Physical Review B, 68, 094101.

Wirth, R., Dobrzhinetskay, L., Harte, B., Schreiber, A., and Green, H.W. (2014) High-Fe (Mg,Fe)O inclusion in diamond apparently from the lowermost mantle. Earth and Planetary Science Letters, 404, 365–375.

608 Woodland, A.B., Frost, D.J., Trots, D.M., Klimm, K., and Mezouar, M. (2012) In situ
609 observation of the breakdown of magnetite (Fe_3O_4) to Fe_4O_5 and hematite at high pressures and
610 temperatures. American Mineralogist, 97, 1808-1811.
611
612 Woodland A., Uenver-Thiele, L., and Boffa Ballaran, T. (2015) Synthesis of Fe_5O_6 and the high-
613 pressure stability of Fe^{2+}-Fe^{3+}-oxides related to Fe_4O_5. Goldschmidt Abstracts, 3446.
614
615 Yamanaka, T., Uchida, A., and Nakamoto, Y. (2008) Structural transition of post-spinel phases
616 $CaMn_2O_4$, $CaFe_2O_4$ and $CaTi_2O_4$ under high pressures up to 80 GPa. American Mineralogist, 93,
617 1874-1881.

618

619 **Figure captions**

620

621 Figure 1. BSE image of a) a large crystal of $Mg_2Fe_2O_5$ (experiment H3975; crystal structure
622 published in Boffa-Ballaran et al. 2015) in comparison with b) fine grained Fe_2O_3 + MgO
623 (experiment M569).
624

625 Figure 2. Position of the boundary between $MgFe_2O_4$ and the MgO + Fe_2O_3 phase fields as a
626 function of pressure and temperature. The phase boundary of Levy et al. (2004) and that
627 calculated from the Holland and Powell (2011) database are plotted for comparison. All symbols
628 are experiments from this study. A representative error bar in terms of pressure and temperature
629 is given in the legend for reference.

Figure 3. Phase diagram for magnesioferrite between 8-18 GPa and 900-1600°C. Errors in pressure and temperature are 0.5 GPa and ±30-50°C, respectively (Keppler and Frost 2005). Also shown in gray are the phase boundaries proposed by Levy et al. (2004). Above 1200°C, magnesioferrite breaks down to Fe_2O_3 and an unquenchable, Mg-rich phase. At higher pressures (>14 GPa) the assemblage $Mg_2Fe_2O_5$ + Fe_2O_3 becomes stable (see text). UQ: unquenchable phase

Figure 4. a) Backscatter image of sample V841o exhibiting large crystals of hematite surrounded by the unquenchable phase with mottled texture. b) Experiment M553 exhibits the "unquenchable" phase. Grain boundaries of larger crystals with triple junctions can be observed indicating equilibrium conditions at given pressure and temperature of the experiment. Abbreviations: hem = hematite, mgs = magnesite. c) Backscatter image of sample M551 illustrating the texture of the "unquenchable" phase, which decomposed to MgO and Fe_2O_3.

Figure 5. a) Dark-field TEM image of the unquenchable phase in sample M568, illustrating vermicular intergrowths. The domains with white contrast correspond to Fe-enriched magnesioferrite. The inset is an iron elemental map of the squared area. The STEM-EDX map of Fe concentrations denotes two intimately intergrowth phases with different compositions. b) A high resolution TEM image of a fine mixture of MgO (periclase) and $MgFe_2O_4$ (magnesioferrite), indicating a topotactic relationship of their lattice fringes of oxygen close-packed planes (white arrow heads). c) Fast Fourier Transform (FFT) pattern from image of the Fe-rich domain, indexed as a cubic spinel structure. d) FFT pattern from the Mg-rich domain, indexed as having the rock salt (rs) structure. Some additional diffraction spots, e.g., d = 0.26 nm originate from the Fe-rich domain.

Figure 6. The MgO-$FeO_{1.5}$ binary with stoichiometries of known and hypothetical phases indicated.

Figure 7. Chemical compositions of representative run products plotted in terms of their MgO and FeO contents in weight %. Plotted are hematite, magnesioferrite (O_4) and $Mg_2Fe_2O_5$ (O_5) as quenchable phases and bulk chemical analyses of the unquenchable phases that are consistent with the hypothetical stoichiometries of $Mg_3Fe_2O_6$ (O_6), $Mg_4Fe_2O_7$ (O_7), $Mg_5Fe_2O_8$ (O_8), $Mg_6Fe_2O_9$ (O_9) or $Mg_{11}Fe_2O_{14}$ (O_{14}).

Figure 8. Comparison of powder X-ray diffraction patterns of $Mg_2Fe_2O_5$ and $MgFe_2O_4$.

Figure 9. a) Variation in Mg content (cations per formula unit, c.p.f.u.) in hematite as a function of temperature of the experiment. Systematic variations in molar volume, b), and the lattice parameters, c) and d), as a function of measured Mg content in hematite. Error bars represent uncertainties from refinement of the powder diffraction patterns. Where there are no error bars, the errors are about the size of the symbol.

Figure 10. Comparison of the conditions of the breakdown of spinel-structured phases in several end member compositions. Stability fields for the constituent oxide and $A_2B_2O_5$ + M_2O_3 assemblages are also displayed in systems where they are stable. Data sources: hercynite ($FeAl_2O_4$), Schollenbruch et al. (2009); magnetite (Fe_3O_4), Woodland et al. (2012); chromite

677 ($FeCr_2O_4$), Ishii et al. (2014); magnesiochromite ($MgCr_2O_4$), Ishii et al. (2015), spinel

678 ($MgAl_2O_4$), Akaogi et al. (1999) and Enomoto et al. (2009).

679

680

681

682

683

684

685

686

687

688

689

690

691

692

693

694

695

696

697

This is a preprint, the final version is subject to change, of the American Mineralogist (MSA)
Cite as Authors (Year) Title. American Mineralogist, in press.
(DOI will not work until issue is live.) DOI: http://dx.doi.org/10.2138/am-2017-5871

Table 1. Experimental conditions and run products, including unit-cell parameters of magnesioferrite.

Experiment	starting material	pressure [GPa]	temperature [°C]	run duration [h]	run products[1]	Unit-cell parameter of $MgFe_2O_4$ [Å]
M573	$MgO + Fe_2O_3$	8	900	20	per + hem	-
M585	10% $MgFe_2O_4$ + 90% MgO+ Fe_2O_3	8	900	24	per + hem	-
M518	$MgFe_2O_4$	8	1100	5.5	mf	8.3808(1)
M517	$MgFe_2O_4$	8	1300	5.5	mf	8.3826(2)
M592	10% $MgFe_2O_4$ + 90% MgO+ Fe_2O_3	8	1500	2	mf	8.3810(4)
M577	$MgFe_2O_4$ syn.	9	900	24	per + hem	-
M593	10% $MgFe_2O_4$ + 90% MgO+ Fe_2O_3	9	1000	18	per + hem	-
V862o	$MgO + Fe_2O_3$	9	1100	5.5	mf	8.3824(2)
V862u	$MgFe_2O_4$	9	1100	5.5	mf	8.3799(1)
V864o	$MgFe_2O_4$	9	1300	4.5	mf	8.3814(0)
V864u	$MgO + Fe_2O_3$	9	1300	4.5	mf	8.3812(2)
V865o	$MgO + Fe_2O_3$	9	1300	1.5	mf	8.3820(0)
V865u	$MgFe_2O_4$	9	1300	1.5	mf	8.3812(2)
M594	10% $MgFe_2O_4$ + 90% MgO+ Fe_2O_3	9	1500	3	mf	8.3807(2)
M569	$MgFe_2O_4$	10	1000	17	per + hem	-
M588	10% $MgFe_2O_4$ + 90% MgO+ Fe_2O_3	10	1200	5	per + hem	-
V841o	$MgO + Fe_2O_3$	10	1300	5.5	UQ-O_7 + UQ-O_8 + hem	-
M553	$2MgO + Fe_2O_3$	10	1400	4	UQ-O_7 + hem	-
M629	$MgFe_2O_4$	10	1500	3	mf + hem + UQ-O_6 + (mgs)	-
M633	$MgFe_2O_4$	10	1600	1.5	mf + UQ-O_6	8.3794(7)
M632	$MgFe_2O_4$	11	1300	4.5	hem + UQ-O_{14}	-
M631	$MgFe_2O_4$	11	1450	4	hem + UQ-O_8	-
M616	$MgFe_2O_4$	11	1600	2	O_5 + hem	-
M630	$MgFe_2O_4$	12	1350	4	hem + UQ-O_{14}	-
M568	$MgO + MgFe_2O_4$	12	1400	5	UQ-O_8 + hem	-
M583	$MgFe_2O_4$	12	1500	4	UQ-O_7 + O_5 + hem	-
M590	$MgFe_2O_4$	13	1200	4	per + hem	-
M617	$MgFe_2O_4$	13	1400	5.5	O_5 + hem + UQ-O_9	-
M551	$2MgO + Fe_2O_3$	13	1500	3.5	UQ-O_7 + hem	-
Z1463o	$MgFe_2O_4$	14	1400	3	O_5 + hem	-
Z1461o	$MgFe_2O_4$	16	1300	3	per + hem + O_5	-
H3889	$MgFe_2O_4$	18	1300	5.5	O_5 + hem + (mgs)	-
H4084	$MgO + MgFe_2O_4$	18	1200	4.5	per + hem	-

[1]per: periclase; hem: hematite; mf: magnesioferrite; (mgs): traces of magnesite; O_5: $Mg_2Fe_2O_5$; UQ-O_6: unquenchable phase with a stoichiometry of $Mg_3Fe_2O_6$; UQ-O_7: unquenchable phase with a stoichiometry of $Mg_4Fe_2O_7$; UQ-O_8: unquenchable phase with a stoichiometry of $Mg_5Fe_2O_8$; UQ-O_9: unquenchable phase with a stoichiometry of $Mg_6Fe_2O_9$; UQ-O_{14}: unquenchable phase with a stoichiometry of $Mg_{11}Fe_2O_{14}$

698

699

700

Table 2. Representative electron microprobe data of experimental run products. Abbreviations as in Table 1. "b.d.l.": below detection limit, "n.a.": not analysed

Sample	H3889			M517	M518	M551		M553		M568			
MgO	2.99	48.54	32.28	21.22	22.17	50.53	3.49	2.82	49.61	55.87	56.39	2.39	2.42
FeO	85.95	1.33	62.39	72.49	71.41	44.58	86.24	86.5	45.53	41.56	41.33	87.43	87.79
PtO_2	b.d.l.	0.05	0.13	b.d.l.	0.21	b.d.l.	b.d.l.	b.d.l.	b.d.l.	b.d.l.	0.03	0.02	b.d.l.
Totals	88.94	49.92	94.80	93.71	93.79	95.11	89.73	89.32	95.14	97.43	97.75	89.84	90.21
comment	hem	mgs	$Mg_2Fe_2O_5$	mf	mf	UQ-O_7	hem	hem	UQ-O_7	UQ-O_8	UQ-O_8	hem	hem

701

Sample	M569		M573	M577		M583			M588	M590	M592	
MgO	0.66	99.55	0.61	0.45	99.87	50.54	2.94	33.56	1.45	1.67	21.72	21.55
FeO	89.18	1.94	89.04	89.90	1.76	46.97	87.82	63.52	89.00	88.83	72.78	72.58
PtO_2	b.d.l.	b.d.l.	0.11	b.d.l.	b.d.l.	b.d.l.	b.d.l.	b.d.l.	b.d.l.	b.d.l.	b.d.l.	0.03
Totals	89.84	101.49	89.76	90.35	101.63	97.51	90.76	97.08	90.45	90.50	94.50	94.16
comment	hem	MgO	hem	hem	MgO	UQ-O_7	hem	$Mg_2Fe_2O_5$	hem	hem	mf	mf

702

Sample	m594		m616		M617			M629				M630
MgO	21.01	21.05	3.04	32.95	2.09	33.61	61.86	21.64	2.92	48.40	45.11	76.59
FeO	72.41	72.76	86.12	63.05	87.69	62.70	36.39	73.38	88.29	1.32	51.24	24.01
PtO_2	b.d.l.	0.01	b.d.l.	b.d.l.	b.d.l.	b.d.l.	b.d.l.	0.06	b.d.l.	b.d.l.	0.05	b.d.l.
Totals	93.42	93.82	89.16	96.00	89.78	96.31	98.25	95.08	91.21	49.72	96.40	100.60
comment	mf	mf	hem	$Mg_2Fe_2O_5$	hem	$Mg_2Fe_2O_5$	UQ-O_9	mf	hem	mgs	UQ-O_6	UQ-O_{14}

703

Sample	M631		M632	M633		V841o				V862o		V862u
MgO	55.30	2.19	75.87	44.67	21.17	50.49	49.17	2.49	54.83	22.51	22.49	21.84
FeO	41.02	87.98	24.05	49.22	70.74	44.73	1.72	87.39	41.54	71.59	72.23	71.20
PtO_2	0.00	0.00	0.08	0.25	0.03	n.a.	n.a.	n.a.	n.a.	0.02	0.00	0.00
Totals	96.32	90.17	100.00	94.14	91.94	95.22	50.89	89.88	96.37	94.12	94.72	93.04
comment	UQ-O_8	hem	UQ-O_{14}	UQ-O_6	mf	UQ-O_7	mgs	hem	UQ-O_8	mf	mf	mf

704

Sample	V864o	V864u	V865u	V865o	Z1461o		Z1463o	
MgO	21.95	21.77	22.14	21.69	1.59	32.34	32.54	2.67
FeO	72.45	72.13	71.16	70.93	89.88	64.77	64.17	88.29
PtO_2	0.00	0.00	n.a.	n.a.	0.00	0.00	0.00	0.00
Totals	94.40	93.90	93.30	92.62	91.47	97.11	96.71	90.96
comment	mf	mf	mf	mf	hem	$Mg_2Fe_2O_5$	$Mg_2Fe_2O_5$	hem

This is a preprint, the final version is subject to change, of the American Mineralogist (MSA)
Cite as Authors (Year) Title. American Mineralogist, in press.
(DOI will not work until issue is live.) DOI: http://dx.doi.org/10.2138/am-2017-5871

Table 3. Unit-cell parameters of MgO. Uncertainties in brackets are those returned by the GSAS refinement.

Sample	MgO	
	a **[Å]**	**V [Å^3]**
M569	4.2120(1)	74.726(6)
M573	4.2120(2)	74.72(1)
M577	4.2118(1)	74.714(7)
M585	4.2119(8)	74.72(4)
M588	4.2109(1)	74.666(6)
M590	4.2112(2)	74.683(9)
M593	4.2118(2)	74.716(10)
H4084	4.2120(1)	74.724(4)

Table 4. Possible Fe-Mg oxide stoichiometries matched with their expected compositions as measured by bulk microprobe analysis.

EPMA analysis [wt%]		possible stoichiometry
FeO	**MgO**	
72(1)	21(1)	$MgFe_2^{3+}O_4$
63(1)	33(1)	$Mg_2Fe_2^{3+}O_5$
51(1)	44(1)	$Mg_3Fe_2^{3+}O_6$
46(1)	50(1)	$Mg_4Fe_2^{3+}O_7$
41(1)	56(1)	$Mg_5Fe_2^{3+}O_8$
36(1)	61(1)	$Mg_6Fe_2^{3+}O_9$
24(1)	76(1)	$Mg_{11}Fe_2^{3+}O_{14}$

This is a preprint, the final version is subject to change, of the American Mineralogist (MSA)
Cite as Authors (Year) Title. American Mineralogist, in press.
(DOI will not work until issue is live.) DOI: http://dx.doi.org/10.2138/am-2017-5871

Table 5. Unit-cell parameters of $Mg_2Fe_2O_5$. Uncertainties in brackets are those returned by the GSAS refinement.

Sample	$Mg_2Fe_2O_5$			
	a **[Å]**	***b*** **[Å]**	***c*** **[Å]**	**V [Å^3]**
M616	2.8863(16)	9.730(6)	12.540(6)	352.16(20)
M617	2.8870(4)	9.7225(15)	12.5527(15)	352.34(6)
H3889	2.8858(2)	9.7187(9)	12.5476(9)	351.91(3)
Z1461o	2.8884(7)	9.7253(25)	12.5468(26)	352.45(9)
Z1463o	2.8872(2)	9.7228(8)	12.5523(9)	352.36(3)

710

711

712

Table 6. Unit-cell parameters and molar volume of hematite as well as the Mg-content in hematite

Experiment	hematite			
	a**[Å]**	***c*** **[Å]**	**V [Å^3]**	**Mg content (c.p.f.u.)**
H3889	5.0482(2)	13.7873(7)	304.284(16)	0.1191(12)
M551	5.0579(2)	13.798(1)	305.688(28)	0.1377(12)
M573	5.0383(1)	13.7601(6)	302.496(13)	0.0243(5)
M568	5.0451(2)	13.7841(7)	303.847(15)	0.0952(11)
M569	5.0409(1)	13.7608(3)	302.824(7)	0.0262(6)
M577	5.0377(1)	13.7555(3)	302.326(7)	0.0177(5)
M585	5.0392(3)	13.763(2)	302.68(4)	0.0229(5)
M588	5.0399(1)	13.7639(3)	302.767(8)	0.0571(8)
M590	5.0426(1)	13.7708(7)	303.249(15)	0.0656(9)
M616	5.0445(4)	13.792(2)	303.96(3)	0.1208(12)
M617	5.0433(2)	13.7798(7)	303.527(15)	0.0826(10)
M630	5.0424(1)	13.7737(5)	303.291(11)	0.0785(10)
M631	5.0435(1)	13.7826(6)	303.622(14)	0.0862(10)
M632	5.0433(1)	13.7765(6)	303.463(14)	0.0768(10)
V841o	5.0469(1)	13.7778(8)	303.927(17)	0.0983(11)
Z1461o	5.0418(1)	13.7707(3)	303.146(6)	0.0618(9)
Z1463o	5.0438(2)	13.7792(7)	303.580(16)	0.1041(11)

713

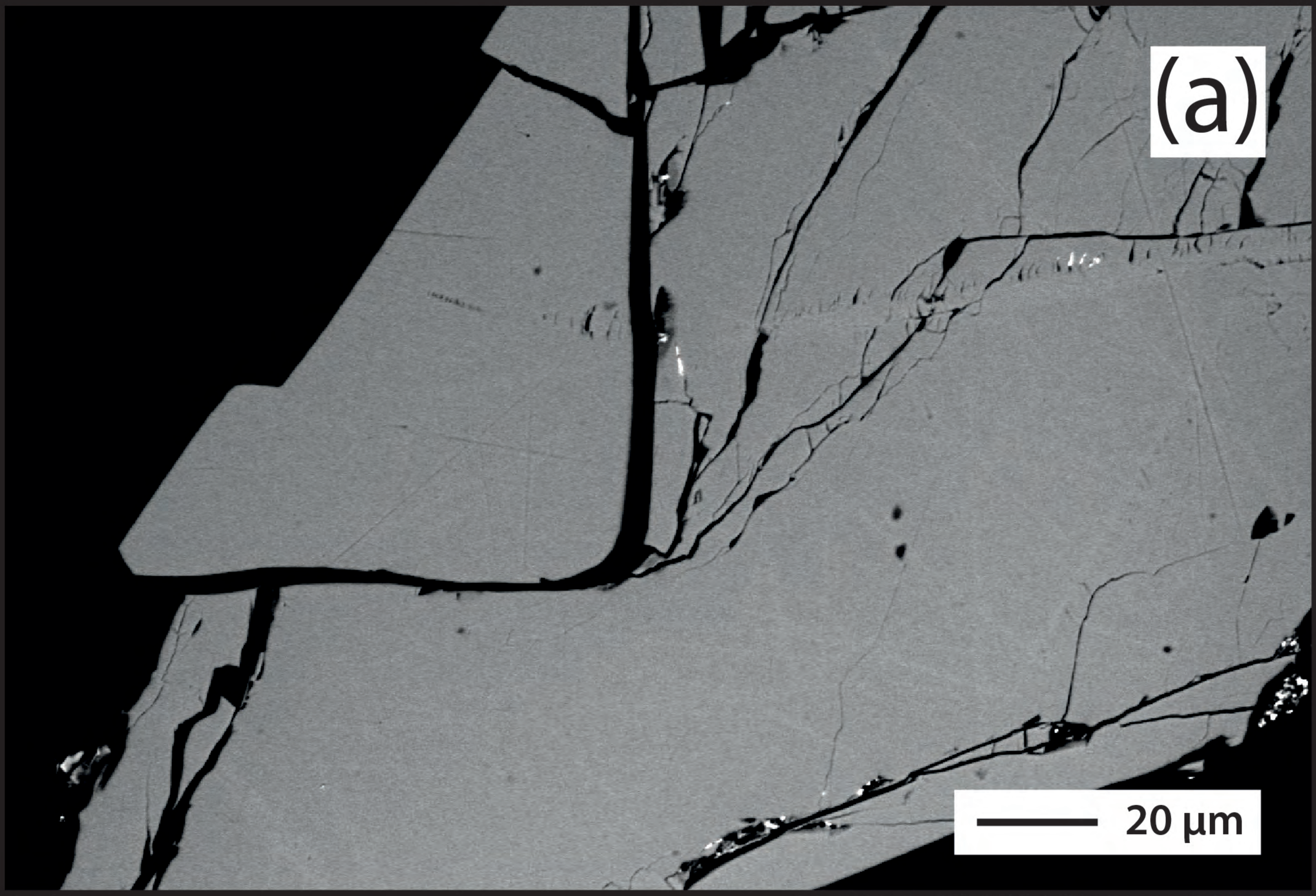
(a)
20 µm

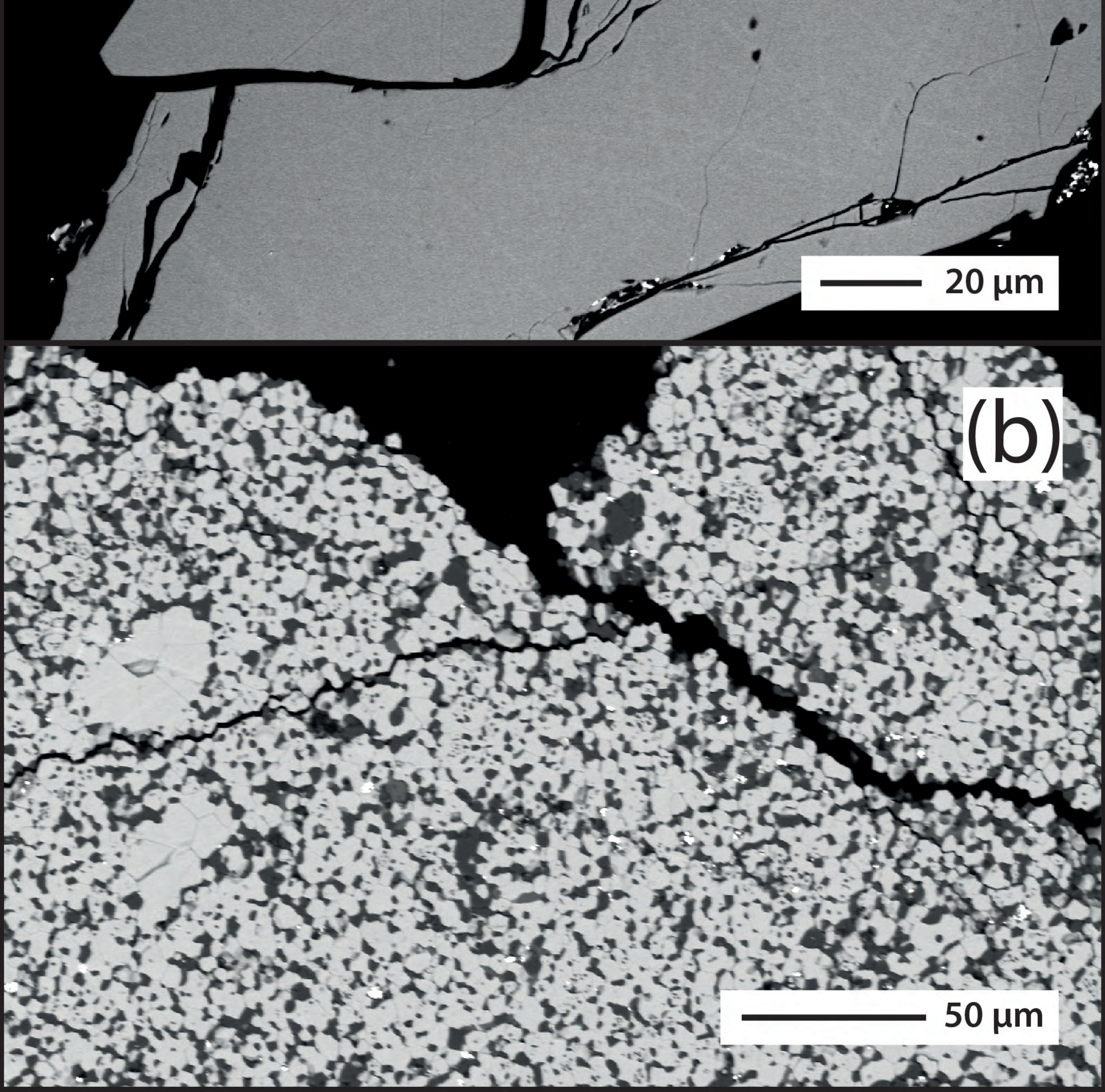
(b)
50 µm

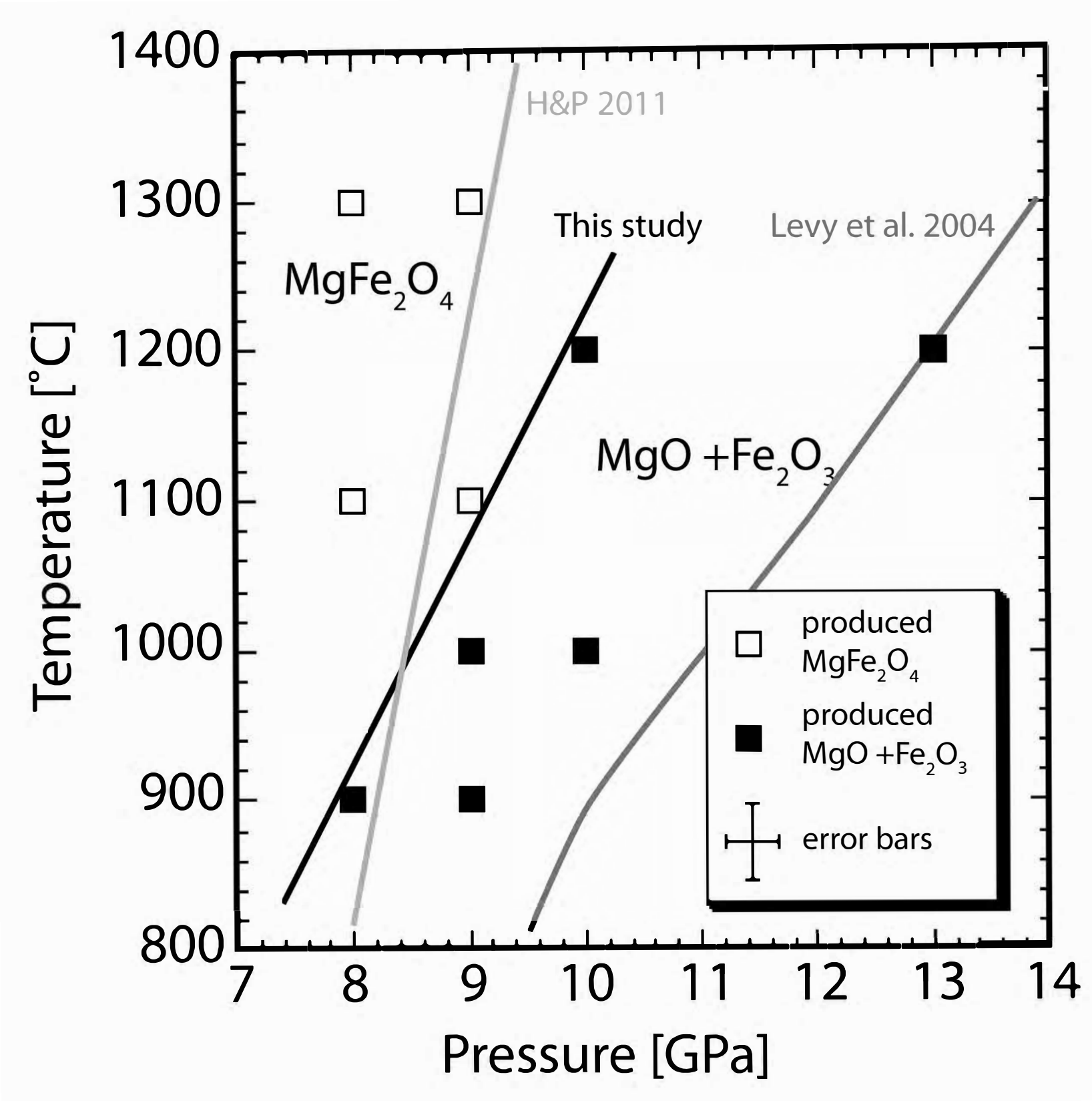
1400
1300
1200
1100
1000
900
800
Temperature [°C]
7
8
9
10
11
12
13
14
Pressure [GPa]
H&P 2011
This study
Levy et al. 2004
MgFe2O4
MgO +Fe2O3
produced MgFe2O4
produced MgO +Fe2O3
error bars

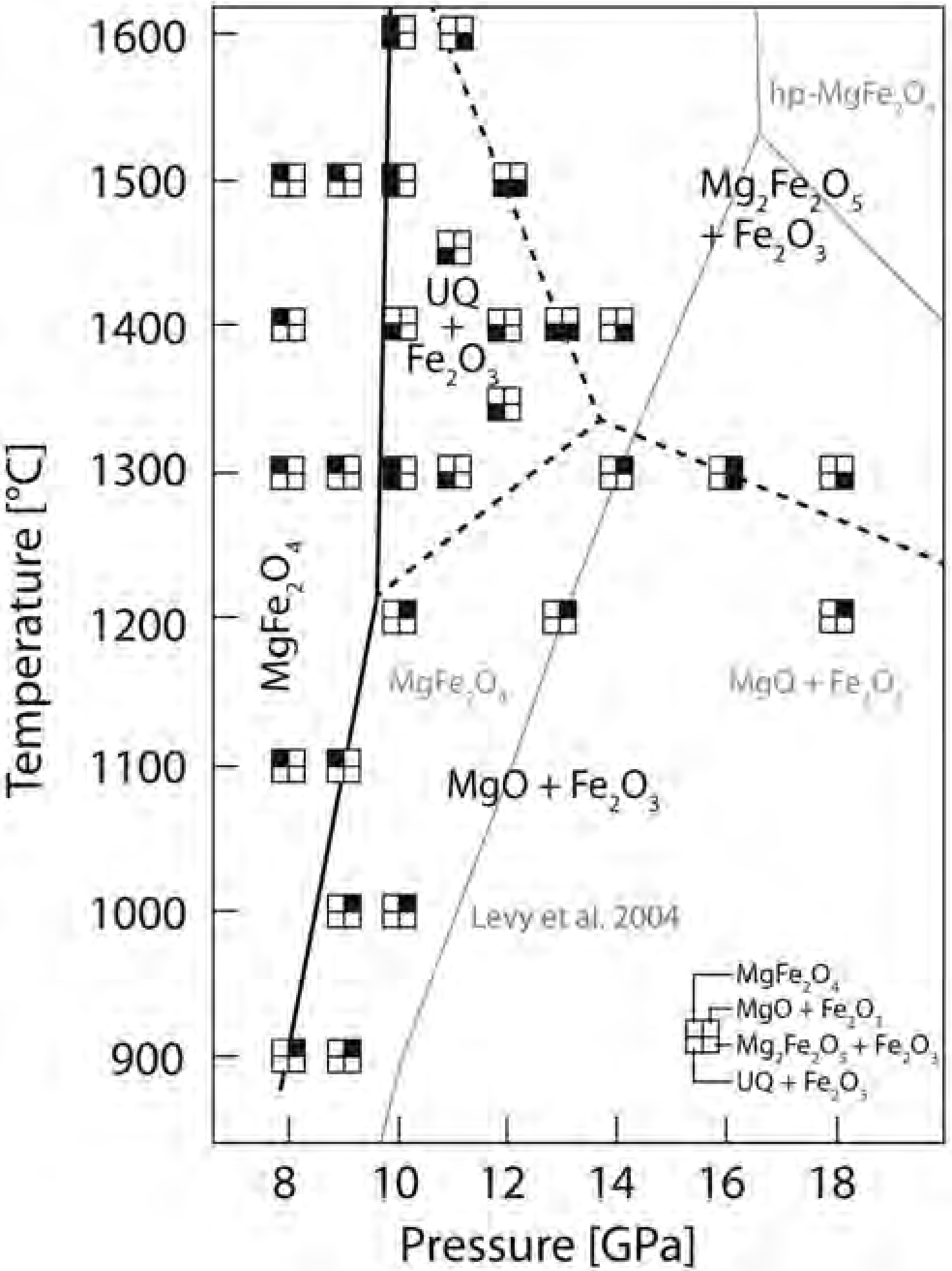
1600
1500
1400
1300
1200
1100
1000
900
Temperature [°C]
8
10
12
14
16
18
Pressure [GPa]
hp-MgFe2O4
Mg2Fe2O5 + Fe2O3
UQ + Fe2O3
MgFe2O4
MgFe2O4
MgO + Fe2O3
MgO + Fe2O3
Levy et al. 2004
MgFe2O4
MgO + Fe2O3
Mg2Fe2O5 + Fe2O3
UQ + Fe2O3

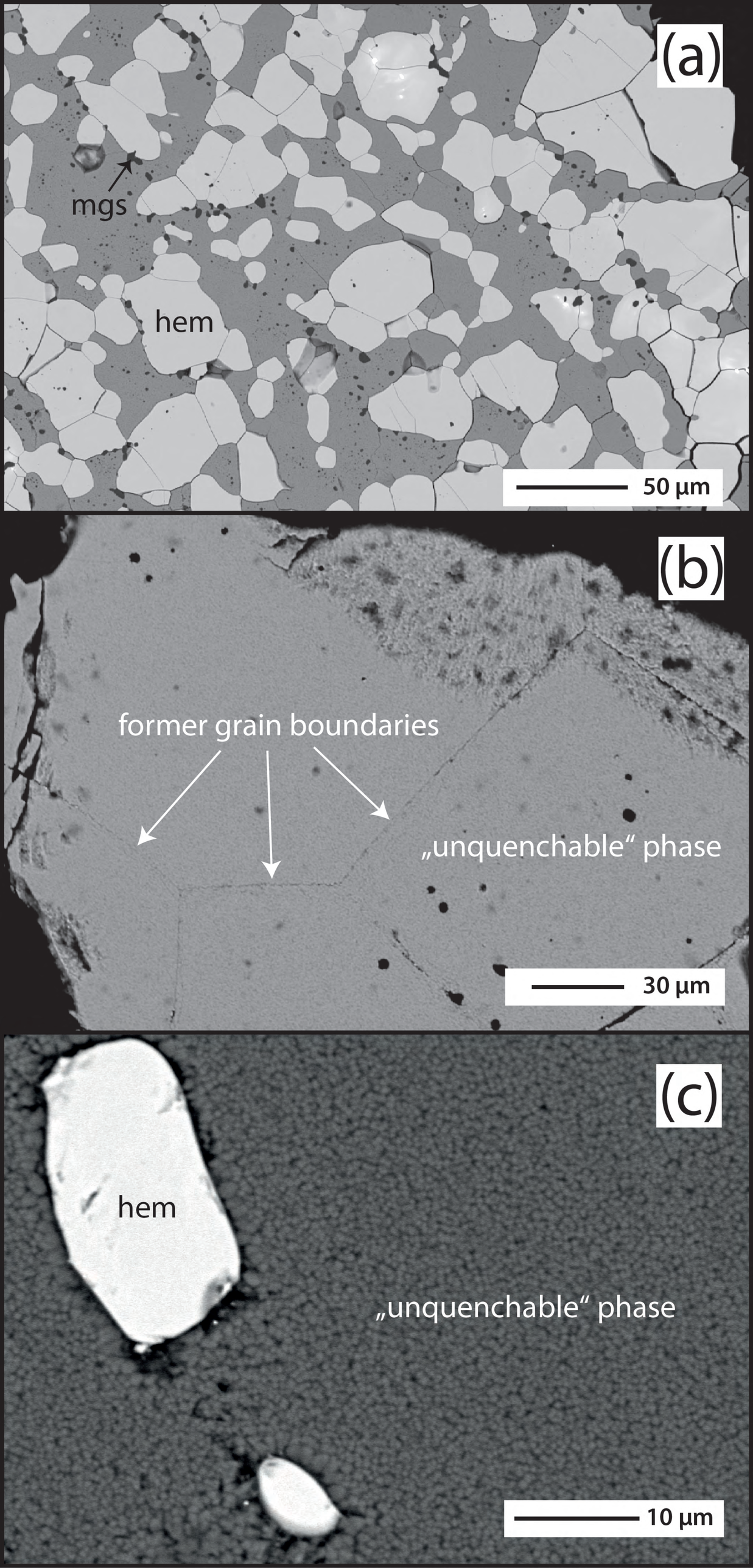
(a)
mgs
hem
50 µm
(b)
former grain boundaries
„unquenchable“ phase
30 µm
(c)
hem
„unquenchable“ phase
10 µm

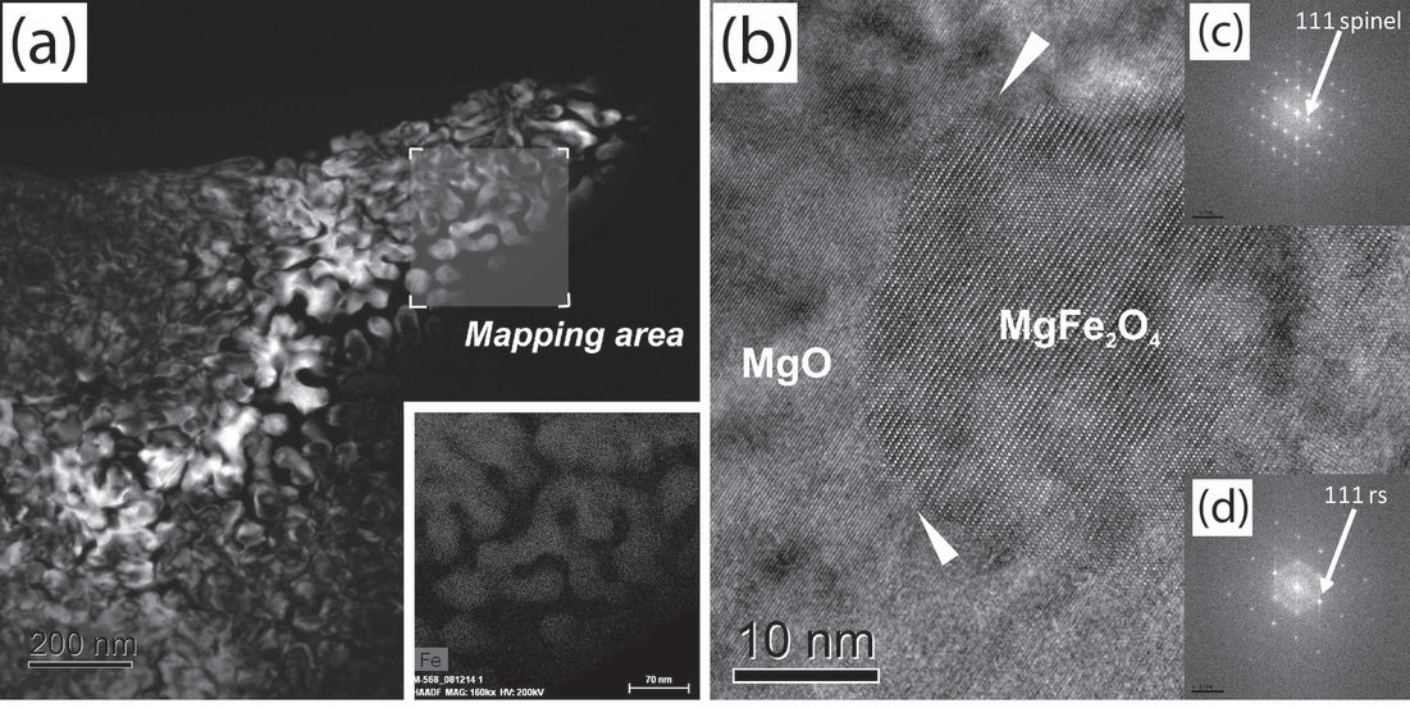
(a)
Mapping area
200 nm
Fe
70 nm
(b)
MgO
$MgFe_2O_4$
10 nm
(c)
111 spinel
(d)
111 rs

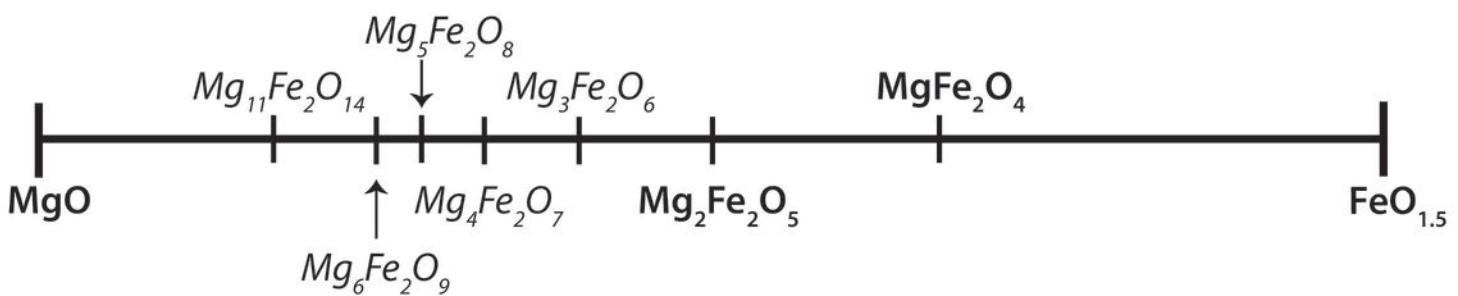
$Mg_5Fe_2O_8$
$Mg_{11}Fe_2O_{14}$
$Mg_3Fe_2O_6$
$MgFe_2O_4$
MgO
$Mg_4Fe_2O_7$
$Mg_2Fe_2O_5$
$FeO_{1.5}$
$Mg_6Fe_2O_9$

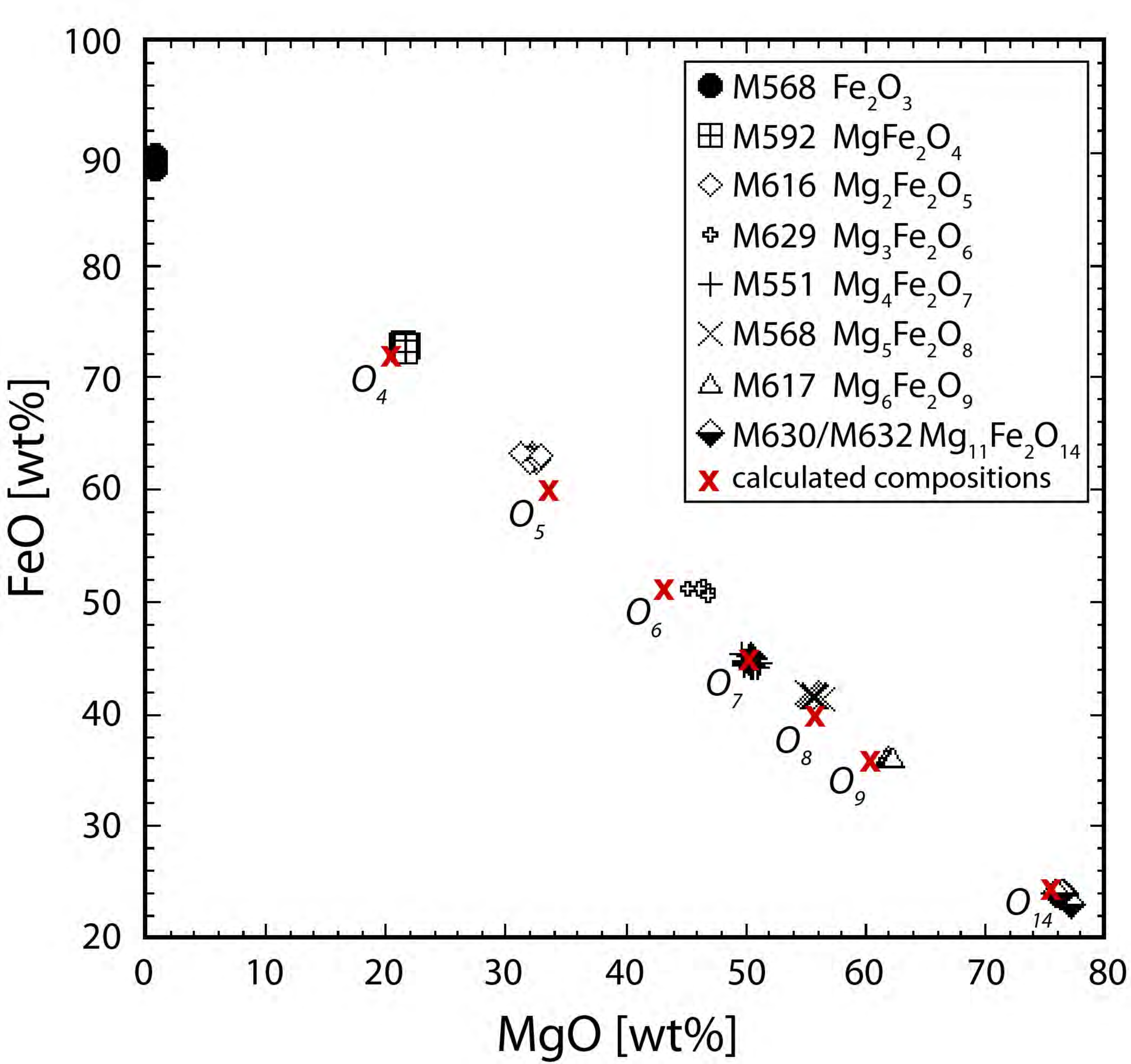
M568 Fe2O3
M592 MgFe2O4
M616 Mg2Fe2O5
M629 Mg3Fe2O6
M551 Mg4Fe2O7
M568 Mg5Fe2O8
M617 Mg6Fe2O9
M630/M632 Mg11Fe2O14
calculated compositions
O4
O5
O6
O7
O8
O9
O14
FeO [wt%]
MgO [wt%]
100
90
80
70
60
50
40
30
20
0
10
20
30
40
50
60
70
80

$Mg_2Fe_2O_5$

V864o.
9 GPa,
~1300 °C

$MgFe_2O_4$

H3975
15 GPa,
~1550 °C

intensity [arbitrary units]

1 2 3 4 5 6 7

d-spacing [Å]

a)

Mg [c.p.f.u.]

Temperature [°C]

b)

molar volume [Å^3]

Mg [c.p.f.u.]

c)

a axis [Å]

Mg [c.p.f.u.]

d)

c axis [Å]

Mg [c.p.f.u.]

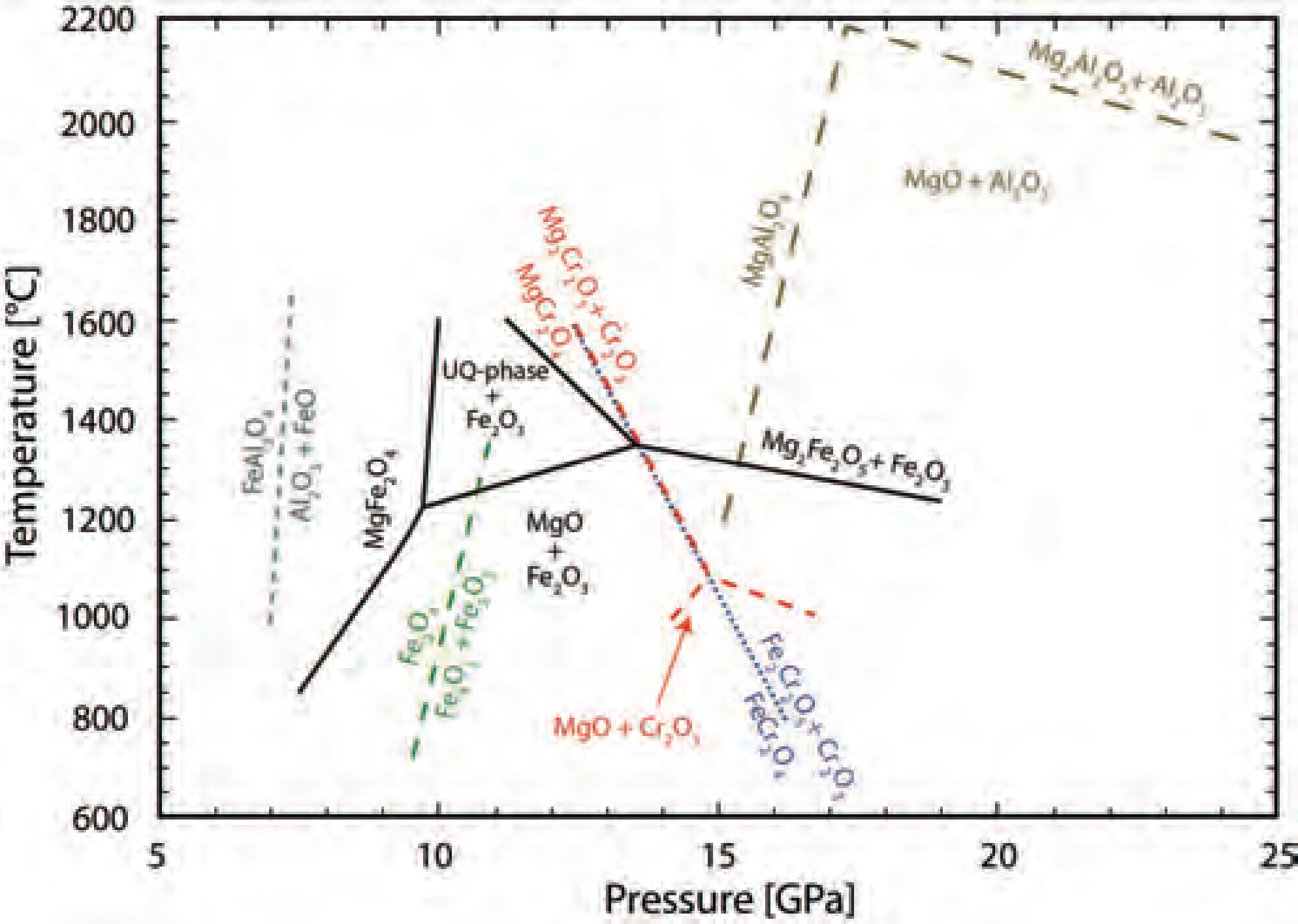
2200
2000
1800
1600
1400
1200
1000
800
600
Temperature [°C]
5
10
15
20
25
Pressure [GPa]
UO-phase
+
Fe2O3
MgFe2O4
MgO
+
Fe2O3
Mg3Fe2O5+ Fe2O3
MgO + Al2O3
Mg2Al2O4+ Al2O3
MgAl2O4
MgO + Cr2O3
FeAl2O4
Al2O3 + FeO